Parallel, linear, and subnanometric 3D tracking of microparticles with Stereo Darkfield Interferometry

Martin Rieu, Thibault Vieille, Gaël Radou, Raphael Jeanneret, Nadia Ruiz-Gutierrez, Bertrand Ducos, Jean-François Allemand, Vincent Croquette

OPTICS

Parallel, linear, and subnanometric 3D tracking of microparticles with Stereo Darkfield Interferometry

Martin Rieu[1,2]*, Thibault Vieille[1,2]*†, Gaël Radou[1,2†], Raphaël Jeanneret[1,2], Nadia Ruiz-Gutierrez[2], Bertrand Ducos[1,2], Jean-François Allemand[1,2], Vincent Croquette[1,2,3‡]

While crucial for force spectroscopists and microbiologists, three-dimensional (3D) particle tracking suffers from either poor precision, complex calibration, or the need of expensive hardware, preventing its massive adoption. We introduce a new technique, based on a simple piece of cardboard inserted in the objective focal plane, that enables simple 3D tracking of dilute microparticles while offering subnanometer frame-to-frame precision in all directions. Its linearity alleviates calibration procedures, while the interferometric pattern enhances precision. We illustrate its utility in single-molecule force spectroscopy and single-algae motility analysis. As with any technique based on back focal plane engineering, it may be directly embedded in a commercial objective, providing a means to convert any preexisting optical setup in a 3D tracking system. Thanks to its precision, its simplicity, and its versatility, we envision that the technique has the potential to enhance the spreading of high-precision and high-throughput 3D tracking.

INTRODUCTION

Video-based three-dimensional (3D) tracking of microparticles has become a major tool revealing the dynamics of microorganism motility (*1*). On the other hand, by allowing to track the position of a microbead attached to a biopolymer, it is essential for the single-molecule characterization of molecular motors such as polymerases or helicases (*2*). Compared to other force spectroscopic techniques such as optical tweezers or atomic force microscopes (AFM), techniques based on 3D tracking present the extremely useful advantage of being parallelizable. However, despite recent notable improvements (*3*–*5*), 3D tracking techniques suffer from the limitation of their precision and from the requirement of object-specific calibrations before any measurement.

The past decade has witnessed substantial improvements (*6*) of microparticle 3D tracking techniques, providing better axial and lateral precision and smaller optical aberrations. However, most of these competing solutions have made improvements solely for one feature. For instance, while some allow subnanometer precision, they are not suited for parallelization (*7*). Others do not allow full-frame real-time tracking, as they rely on very high acquisition rates (*4*, *8*) incompatible with the maximal transfer rate between cameras and computers.

Among these methods, evanescent field–based ones are precise but limited in their detection range, of the order of the wavelength of the exciting light (*9*–*11*). Technologies based on the dependence of the point spread function (PSF) with the axial position (*12*–*20*) allow precise 3D tracking in the far field but suffer from the complexity of their experimental implementation and from their dependence on the quantitative measurement of the image shape that increases their sensibility to optical imperfections such as spherical aberration or astigmatism. The need for lookup tables calibrated for each emitter (or at least for sufficient positions in the field of view) (*6*) limits their throughput and their usage. Tracking of free particles variable in size quickly passing in the field of view is then almost impossible. A significant amelioration of ring-shaped PSFs (*12*, *13*) was recently proposed (*21*), allowing nanoparticle tracking in living cells, but is limited in axial range (a few hundreds of nanometers) and precision (5 to 6 nm).

By comparison, stereoscopic methods (*22*–*24*) are more versatile and proficient in the context of heterogeneous and fast-moving particles. Using two light sources with different incidences, they produce two images coinciding when the particle is in focus. As the tracked object moves out of focus by δz, the shift between both images δx increases linearly with δz. This linearity is a great feature of the method alleviating the requirement of a calibration step and ensuring its independence with respect to the particle size. However, the necessary reduction of the numerical aperture to at least half of the possible angles results in a larger PSF and thus a reduced precision. This loss of information can be, in principle, compensated for by increasing the number of photons used to build their PSF, but the finite well depth (the maximum number of photons treated by one pixel during one frame) of cameras sets a limit to this strategy. At the same time, such a numerical aperture limits the axial measurement range.

Here, we present a method, Stereo Darkfield Interferometry (SDI) (*25*), that combines the linearity and parallelization ability of stereoscopic methods with the high per-photon information content of structured PSF. It thus allows us to optimize the use of the transmission rate and of the well depth of cameras. Furthermore, the technique enables to reach a better compromise between the axial measurement range and the resolution by selecting a small range of incident angles and by using interferometry to structure light and thus to boost precision. Our approach is designed to track, in real time, a large number of diluted microparticles with subnanometer axial and lateral precision with no limit on the duration of the experiments, thus significantly enhancing the throughput of subnanometer 3D single-particle tracking. Furthermore, it allows us to greatly simplify the tracking of free microorganisms by suppressing the need to constitute lookup tables.

[1]Laboratoire de Physique de L'Ecole Normale Supérieure de Paris, CNRS, ENS, Université PSL, Sorbonne Université, Université de Paris, 75005 Paris, France. [2]Institut de Biologie de l'Ecole Normale Supérieure (IBENS), Ecole Normale Supérieure, CNRS, INSERM, Université PSL, 75005 Paris, France. [3]ESPCI Paris, Université PSL, 10 rue Vauquelin, 75005 Paris, France.
*These authors contributed equally to this work.
†Present address: Depixus, 3-5 Impasse Reille, 75014 Paris, France.
‡Corresponding author. Email: vincent.croquette@espci.psl.eu

We illustrate the precision of the method by acquiring, with a camera-based method, traces from force spectroscopic events showing nanometric stepping (helicase stepping and oligonucleotide hybridization), thus paving the way for the multiplexing of measurements that were so far exclusively feasible with optical tweezers or AFM and, for this reason, hardly parallelizable. We then illustrate the versatility of the method by measuring dynamic properties of unicellular algae through the acquisition of their 3D trajectories, thus expanding the utility of our approach to a wide range of applications in biological imaging.

RESULTS

A simple mask in the Fourier plane allows 3D tracking

Figure 1 presents the principle of SDI. Illumination is generated by two superluminescent light-emitting diodes (LEDs) sending collimated parallel beams with symmetric incidence angles of ±39° from the optical axis (Fig. 1A). The microscope is built around an infinitely corrected objective and a field lens producing an image on a camera chip. An afocal system built with four lenses is used to access the image focal plane of the objective that is physically located inside the objective mount. A black absorbant film with slits is used as a filter in the Fourier plane, i.e., the back focal plane. In the absence of diffusing particles, no light reaches the camera as the two illumination beams are focused on the black region located between the slits (Fig. 1B). The Fourier filter is built with four symmetrical slits spanning the x axis. When a micrometer-sized particle is placed in the objective focal plane, the light stemming from each of the sources is diffused in a cone, which mostly covers the two closest slits. The slits select two beams that are focused on the camera chip by a lens placed in contact with the slits. When the particle is at the focal plane, the beams originating from both slit pairs coincide. To separate them along the y direction, we place two glass slides tilted with opposite incidences (±17°) just behind each slit pair in close contact with the imaging lens. Their incidence is chosen to be large enough so that the two images coming from both pairs of slits do not coincide. Because of the double-slit configuration, each of the beam pairs issued from the same light source, as in the so-called Young's double-slit experiment, gives rise to an interferometric pattern. When the object moves away from the focal plane by δz, both patterns are translated in a shear mode with opposite directions along the x axis (Fig. 1, C and D). The distance between each of them is linearly related to the axial displacement δz (figs. S1 to S4), whereas the average of their positions is related to x-y movement of the tracked object, as in (*22*).

Subnanometric precision in all three directions

The structure of the interferometric fringes of SDI increases both the axial and in-plane resolution of the bead position. Assuming a photon-limited noise, the optical noise σ_i on the 3D localization of the bead along the i direction must verify (see text S1)

$$\sigma_i^2 > \frac{1}{g_i^2 N} \frac{1}{\int \frac{f'(i)^2}{f(i)} di} \quad (1)$$

where N is the number of photons received during one frame, f is the profile of the interferometric pattern, and g is the coefficient relating the signal displacement to the displacement of the tracked object. For the transverse displacement, g_x is simply the geometric magnification of the optical system. The axial displacement g_z depends on the magnification and on the angle of the incident light as described by the formula given in text S2.

In practice, for real-time tracking, the number of photons received per second is limited by the transfer rate of the camera and its well depth (maximum number of electrons per pixel). Increasing the spread of a Gaussian PSF results in a loss of precision. However, SDI allows spreading the PSF on several pixels without losing precision (Fig. 1, E to G): The PSF is indeed structured, increasing its spatial derivative and thus the value of the integral in the denominator in Eq. 1. We show in Fig. 1G the experimental and theoretical values of the precision of SDI: The structuration of the signal allows a fourfold improvement of the spatial precision compared to the equivalent unstructured PSF. At the maximum light intensity allowed by the camera well depth, the frame-to-frame error on the position of the tracked objects due to photon noise is as low as 0.2 nm in y and z directions and as 0.1 nm in x direction (Fig. 1H). The difference between z and x axes is due to a difference between the transverse and the axial magnification of the setup (see text S2). The slightly poorer precision in y is due to the asymmetry of the SDI profile pattern (no structure in the y direction of the slits presented in this paper).

Label-free measurements of the kinetics of hybridization of very short oligonucleotides

We now illustrate the precision of our tracking technique through various single-molecule force spectroscopy measurements. These measurements are performed with magnetic tweezers: DNA molecules are attached between a glass surface and a micrometric magnetic bead (Fig. 2, A and B). A force is applied by approaching magnets, while the extension of the DNA molecule is measured by tracking the position of the bead with the help of SDI (Fig. 2C). The following examples are, to our knowledge, the first nanometric measurements of relevant biomolecular effects performed with a camera. They open the possibility to importantly increase the throughput of precise enzymatic measurements and to overcome the lack of parallelization that characterizes high-resolution optical tweezers and AFM.

Figure 2E shows the kinetics of hybridization of short oligonucleotides that were obtained by using the nanometric precision of SDI. A DNA molecule with a short single-stranded (ss) segment is attached between a magnetic microsphere (MyOne) and the surface and pulled at a force of ~13 pN. A free 8–base pair (bp) oligonucleotide complementary to the single-stranded DNA (ssDNA) segment of the tethered molecule is injected in the solution. As the oligonucleotide hybridizes to the molecule, eight bases of the latter are converted from ssDNA to double-stranded DNA (dsDNA), causing a shortening of the molecule of ≈1.5 Å per base at 13 pN, that is a total 1.2-nm extension difference (Fig. 2D). When the oligonucleotide unbinds, the molecule recovers its original length. The resulting two-state (Fig. 2E) dynamics allow characterizing the kinetics of the hybridization process at difference forces between 10 and 20 pN (Fig. 2F).

These nanometric experiments have a temporal resolution close to the second, the latter being limited by physical reasons related to the bead explained in text S3. For signals of larger spatial amplitude, the temporal resolution is drastically improved. For hairpin fluctuating between its open and close states, involving differences of extension between the two states of 10 nm, data show well-defined millisecond steps (fig. S5 and text S4).

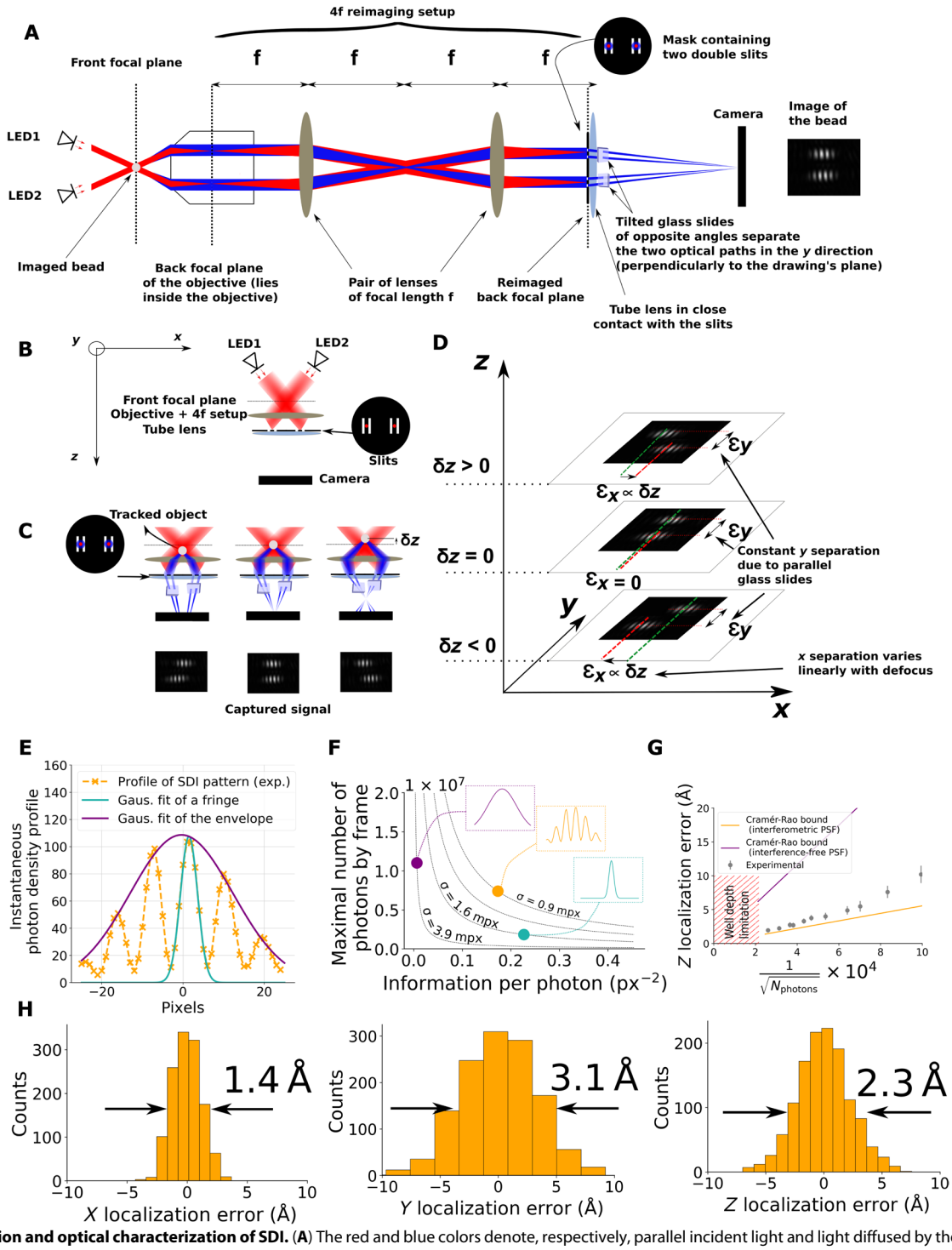

Fig. 1. Description and optical characterization of SDI. (**A**) The red and blue colors denote, respectively, parallel incident light and light diffused by the scatterer (same wavelengths). (**B**) Schematic view of the setup in the absence of scatterer. For the sake of clarity, the objective and the 4f setup are represented as a unique lens. The incoming parallel light is blocked, ensuring dark field. (**C**) When a scatterer is present, the light goes through the slits and creates a PSF consisting of two interference patterns. (**D**). Vertical stack of the SDI images (objective, 100×) as a function of the defocus (axial position *z*) of the tracked object. The transverse distance ϵ_x between the two spots is proportional to the defocus (fig. S2). (**E**) Typical transverse density profile of an SDI pattern. One fringe and the envelope are being fitted by Gaussians (Gaus.). (**F**) Theoretical number of photons by frame and information per photon for each profile shown in (E). Interferences allow us to increase the number of photons while keeping a good precision. Thin black lines join points with equal theoretical precision σ (values in millipixels). (**G**) SD of the measured axial position of a microsphere as a function of light intensity (objective, 100×). This is compared with the theoretical Cramér-Rao bounds computed from the experimental profile drawn in *d* and its envelope. The maximal light intensity is constrained by the camera's well depth (here, 30,000 electrons per pixel). (**H**) Distribution of the inferred 3D-positions, at maximal light intensity, of stuck microspheres. A total of 1280 frames are analyzed. No averaging is performed. The mechanical and thermal drifts are subtracted to assess the optical noise of the setup (see Materials and Methods).

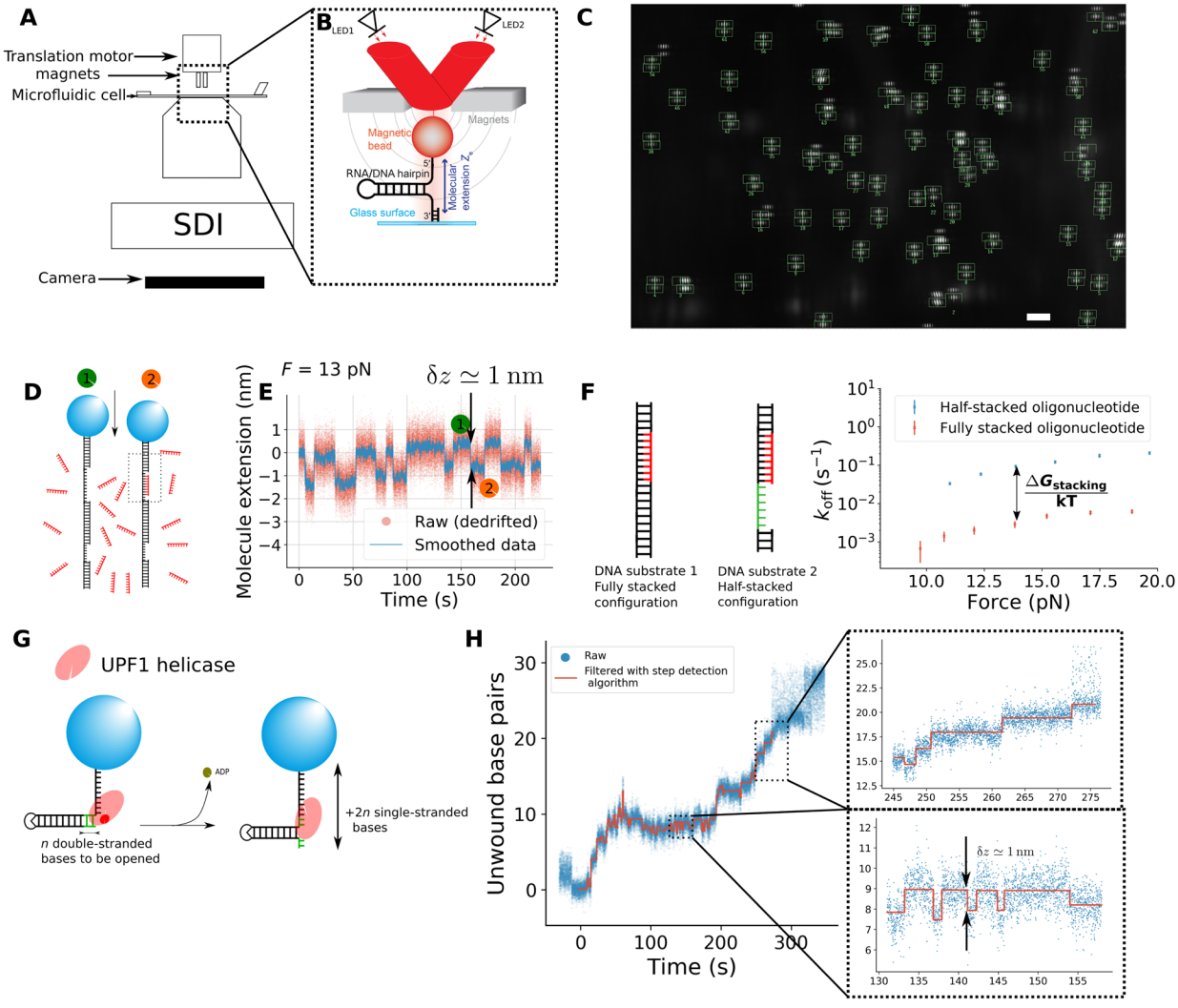

Fig. 2. Application of SDI to nanometric force spectroscopy. (**A**) Schematic representation of the SDI setup attached to magnetic tweezers. (**B**) In this picture, the bead is tracked with SDI. Its *z* position is directly related to the number of bases hybridized in the hairpin. The magnets are designed so that both light sources go through the gap between them. (**C**) Typical field of view. Each pair of fringes, materialized by two green boxes, corresponds to one magnetic bead. Scale bar, 10 μm. (**D**) The hybridization of an 8-bp oligonucleotide causes a shortening of the DNA molecule of typically 1 nm since dsDNA is shorter than ssDNA above 5 pN. (**E**) The 1-nm steps caused by the oligonucleotide hybridization are measured by tracking the position of the magnetic microsphere with the SDI. Figure S6 shows that the binding rate increases linearly with the concentration of oligonucleotide. (**F**) Two DNA substrates are tested with the same oligonucleotide: In the configuration on the left, there is no free base when the oligonucleotide hybridizes. The analysis of the kinetic parameters of the two-level systems described above allows accessing the stacking free energy by comparing k_{off} and k_{on} in both configurations. k_{on} being equal for both configurations (see fig. S7), k_{off} contains all the information about the free energy of stacking. (**G**) Description of the helicase stepping experiment. As the helicase Upf1 unwinds a base pair of the hairpin, the measured extension increases by twice the length of a sDNA base, that is, roughly 0.9 nm at 9 pN. ADP, adenosine diphosphate. (**H**) While unwinding the dsDNA recursively, Upf1 displays discrete steps (top inset). At the stalling position, Upf1 displays a ratchet-like behavior, going forth and back by steps of 1 bp (bottom inset).

Precise single-molecule measurement of the energetics of base stacking

Base stacking is an interaction between the aromatic rings of successive nucleic acids and is a major contributor, alongside the hydrogen bonds between complementary bases, to the stability of the duplex structure (*26*). We used the precision of SDI to investigate the effect of the stacking of the oligonucleotide with the neighbor dsDNA. For this purpose, we reproduced the experiment described above on two different substrates (Fig. 2F). On one of them, the fully stacked configuration, the oligonucleotide hybridizes with an ss gap whose size is exactly 8 bp. On the other, the half-stacked configuration, the ss gap is larger (14 bp) than the oligonucleotide, thus preventing stacking interaction on one of the free ends of the ss fragment. While a similar experiment was pioneered by Whitley *et al.* (*27*) using fluorescence resonance energy transfer, we here are able to perform it in a fluorescence-free setup, thus avoiding an eventual bias that could be introduced by the interaction between the fluorescent label and the DNA. From the difference in the measured hybridization kinetics between the two substrates (Fig. 2F), we notably extract the free energy of stacking (fig. S8) and find $\Delta G_{\text{stacking, AG}} = 2.0 \pm 0.2$ kcal/mol. The free energy does not depend on the force in the considered range (12 to 18 pN). This is coherent with the fact

that the elongation of dsDNA is almost constant in this force range. The method could be easily expanded to a more complete characterization of the energetics of these short segments of nucleic acids.

Observation of helicase stepping with magnetic tweezers thanks to SDI

Helicases are essential enzymes that unwind dsDNA to separate the two DNA strands. They are key elements of DNA replication and repair. As a helicase unwinds a DNA hairpin pulled at 9 pN and tethered between a surface and a magnetic bead, the measured elongation increases by twice the length of an ssDNA base for each base pair unwound, that is, roughly 1 nm (see Fig. 2G). Distinguishing individual steps of a helicase with magnetic tweezers thus requires tracking the bead with subnanometric resolution.

On Fig. 2H, we show that the resolution enhancement provided by SDI allows resolving the individual steps of Upf1, provided that the adenosine triphosphate (ATP) concentration is low enough (500 nM). Upf1 is a helicase belonging to the Superfamily 1 that we studied in previous works using magnetic tweezers (*28*, *29*). The 30-bp hairpin is open step by step until the remaining unwound part becomes too short and starts to oscillate spontaneously between its open and closed states under the influence of the applied force and of the thermal fluctuations (starting from 272 s). At some positions, the enzyme displays a ratchet-like behavior with back-and-forth steps of 1 bp. Away from this stalling position, the distribution of step sizes displays intermediate sizes between 1 and 2 bp (cf. fig. S9 and text S5). These intermediate step sizes were already observed in optical tweezer experiments (*30*) and interpreted as an asynchronous release of both stands. Stalling positions of the enzyme are reproducible from beads to beads and can be easily identified even at higher ATP concentration. We show, for example, in fig. S10 a trace of the helicase domain of yeast-Upf1 unwinding a 30-bp hairpin at a concentration of 10 μM ATP and the corresponding distribution blockage positions over 80 single-helicase events (fig. S11). Averaging over these 80 events allows us to determine blockage positions with the resolution of the base pair.

Direct incorporation into a preexisting microscope

SDI can be directly embedded into an objective and thus can be commercially distributed as a 3D tracking module for any preexisting microscope. Because of the technical complexity of planar high-magnification objectives, such an embedding would need to be performed by the objective supplier. However, to demonstrate this possibility, we disassembled a simpler 20× objective and added the SDI slits directly in the back focal plane of the objective. We brought two prisms of opposite angles directly in contact with the slits (Fig. 3, A to C). These prisms produce a phase shift in the Fourier space that translates into a position shift in the real image space, preventing the superimposition of the two interferometric patterns. They play the same role as the parallel slides presented above. In this low-magnification configuration, the precision is micrometric, while the axial depth of view is greatly enhanced with a conserved linear response: The distance between the interferometric fringes depends linearly on the z position over ranges of the order of 150 μm (Fig. 3H). Residues to linearity over such a range lay below 0.8 μm and are shown in fig. S4. Concerning illumination, the angles corresponding to the slits being smaller, one parallel light source is, in this case, sufficient to perform the measurement. The parameters of this configuration are perfectly suited for the 3D tracking of microorganisms.

Axial motility of Chlamydomonas reinhardtii revealed over 150 μm with an embedded SDI objective

We show in Fig. 3E the image of the model microswimmer *Chlamydomonas reinhardtii* acquired with the modified objective. We studied the dynamics of freely swimming algae confined in a microfluidic Hele-Shaw cell (i.e., width and length ≫ height) of thickness ≈150 μm. Filtering out short trajectories (<1.5 s spent in the field of view) and cells with deficient vertical swimming (spanning less than 110 μm in the axial direction), we analyzed the statistics of 117 independent trajectories and found that the dynamic is largely dominated by the presence of confining walls. As illustrated by the typical track in Fig. 3H, most of the cells performed back-and-forth movements between the upper and lower boundaries (see also fig. S12). The distribution of their axial position displays peaks at 20 to 30 μm from the cell limit (Fig. 3I), in accordance with previous 2D horizontal measurements (*31*). Measuring the vertical angle α_z of each of the 117 trajectories within the middle of the chip (for z, between 60 and 90 μm), we found that it is symmetrically distributed around 0 (Fig. 3J) with a clear peak at ≈ ± 25°. This value compares reasonably well with the most probable outgoing angle following wall scattering as measured in (*32*), which shows that after interacting with either wall, the cells keep swimming in the same direction until colliding with the opposite boundary. This is consistent with the long ≈10-s run time extracted from the run-and-tumble dynamics performed by the algae in bulk (*33*), since in our case, it takes, on average, ≈2.5 s to cross the height of the channel. Last, the symmetry observed in the distribution of angles indicates that gravity axis (*34*) does not play any role in this confined configuration, simply because the gravitational torque (*35*) felt by the algae is too small to bias the cell swimming direction over such a short vertical distance.

DISCUSSION

We presented a new 3D tracking method, Stereo Darkfield Interferometry. The dark field allows for a reduction of the background noise, while the stereoscopic aspect allows for the linearity of the measurement, and the interferometry ensures an angström-level resolution. Because of the high information content of the PSF, the method can be performed at relatively low frequencies that are compatible with real-time tracking. The double-slit configuration selects a small range of angles, resulting in an increased depth of field compared to traditional stereoscopy (*22*). These performances are achieved with a simple and thin mask placed in the Fourier plane of the setup that could be embedded in commercial objectives. Making this mask out of a band-stop optical filter instead of cardboard would permit shifting rapidly from bright field to SDI by changing the wavelength of the incoming light.

Regarding its applications to the tracking of microorganisms, the method presents the advantage to be linear and thus to avoid the constitution of lookup tables. However, it must be acknowledged that a large amount of light going scattered by the sample (around 90%) is absorbed by the black filter inside the SDI objective. It means that an intense light should be sent to the sample to get a bright enough signal. This can be problematic for the observation of light-sensitive species. In the case of *Chlamydomonas*, the algae studied in this paper, this problem was overcome by using a wavelength (730 nm) that is thought to be large enough to not disturb the behavior of the organisms.

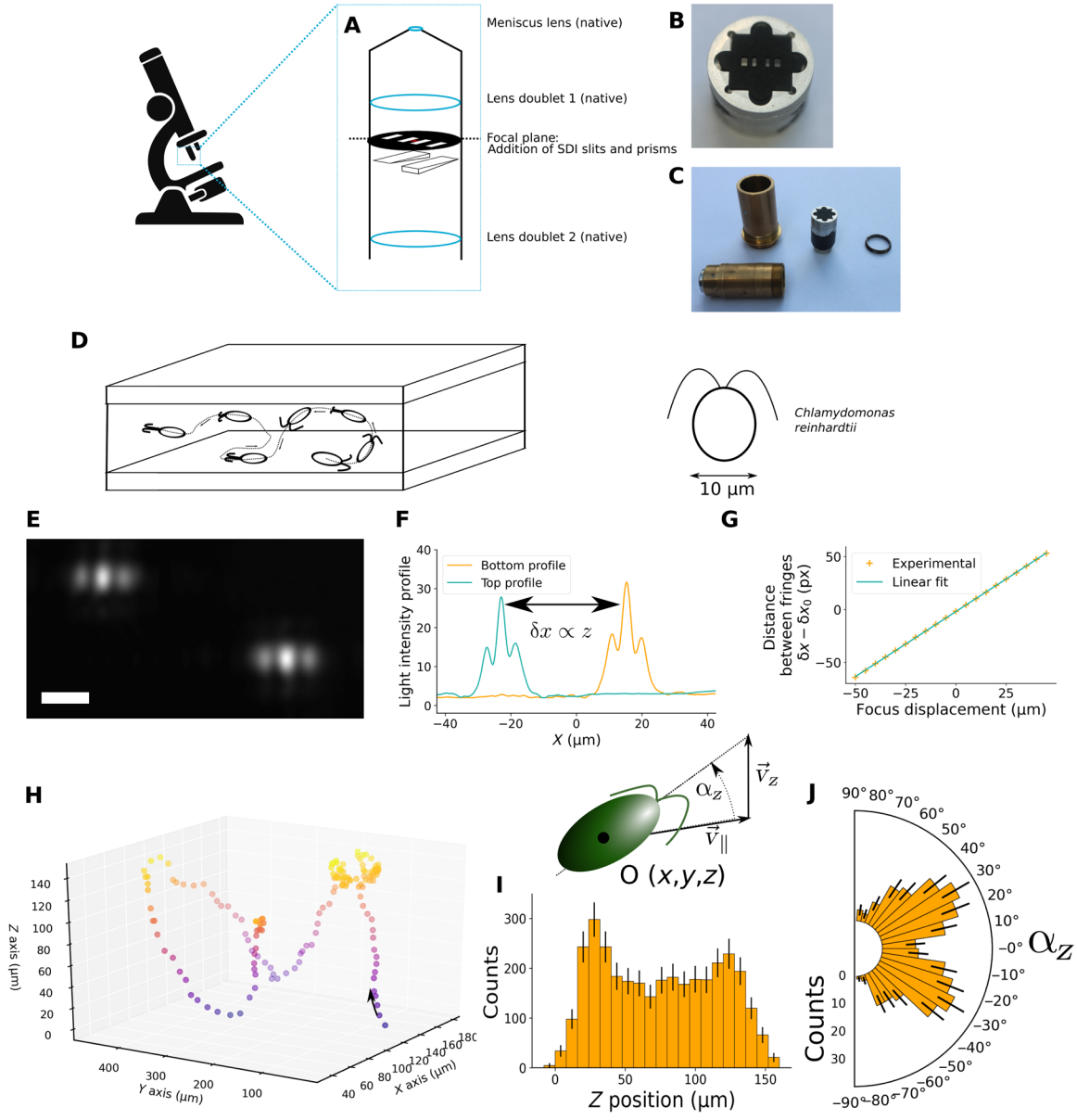

Fig. 3. Application of SDI to single-cell tracking and direct embedding in a commercial objective. (**A**) Schematic description of the modified objective (Olympus, achromatic 20×).The SDI slits brought in contact with two prisms of opposite angles are added in the Fourier plane of the objective. (**B**) Picture of the slits and of the mechanics allowing their insertion in the objective. Photo credit: Vincent Croquette, Laboratoire de Physique de l'Ecole Normale Supérieure. (**C**) Picture of the disassembled objective. Photo credit: Vincent Croquette, Laboratoire de Physique de l'Ecole Normale Supérieure. (**D**) Schematic representation of the tracking experiment: Algae *C. reinhardtii* are inserted in a flow cell containing tris-acetate-phosphate buffer, and their movement is tracked. (**E**) Image of an alga obtained with the integrated objective. White bar, 10 µm. (**F**) Horizontal profile of light intensity corresponding to the image *e*. The lateral shift between the two interference profiles allows measuring the axial position z. (**G**) Dependency of the distance between the interference fringes on the position of the focus for an alga fixed on the surface. (**H**) A 3D trajectory obtained thanks to the SDI modified objective. Acquisition frequency, 10 Hz. Each point corresponds to one frame. Colors represent *z*. (**I**) Distribution of the *z* position of the algae over 3314 positions taken from 117 individual trajectories. (**J**) Distribution of the vertical angles, while an alga crosses the middle of the flow cell (*z* between 60 and 90 µm); 332 crossing events and 117 trajectories.

Regarding its application to magnetic tweezers, the technique allows performing experiments that were so far only possible with hardly parallelizable methods (AFM or optical tweezers) (*30*, *36*, *37*). We showed some preliminary data on helicases (Upf1), but the technique could also be applied to the studies of other enzymes, such as topoisomerases or polymerases. For example, the addition of one base by a polymerase results at 10 pN in the decrease in extension of the DNA molecule by a distance of roughly 1.5 Å. Thus, our optical precision (a frame-by-frame SD of 2 Å in the axial direction due to photon noise) should theoretically allow the distinction of the discrete incorporation of bases by polymerases. However, there is still an obstacle to be overcome that is related to the Brownian motion of the magnetic beads. While we measured the angström-level SD on the position of beads fixed on the glass

surface, this noise increased to the nanometer range (at 160 Hz of acquisition frequency) when the beads were attached to a DNA substrate. This difference is partly due to the magnetic anisotropy (*38*) of the beads as pointed in (*39*), but mainly, it is due to the large increase of the axial hydrodynamic drag applied on the bead caused by the proximity of the surface (*40*). In our case, the correction to the drag is close to factor 15 (see text S3) and thus implies an increase of the integrated Brownian motion of a factor $\sqrt{15} \simeq 4$. As we show in the same supplementary text, this problem cannot be solved by using longer dsDNA handles as the induced loss of stiffness has a worse effect on the noise than the drag coefficient close to the surface. A technological development that could be transposed to magnetic tweezers in the future is the use of extremely stiff handles since they should allow a better spatial separation from the surface without having any notable impact on the stiffness of the construct.

The ability to observe a particle with SDI mainly depends on three parameters: the scattering cross section of the particle at a given wavelength, the position of the slits in the Fourier plane, and the intensity of the incident light. The scattering cross section decreases rapidly with the particle diameter. In practice, the maximum irradiance of the superluminescent LEDs used in our setup (roughly 1 W/cm^2) allows us to track magnetic beads (Ademtech MasterBeads) of 500 nm of diameter with a 2-ms shutter time (fig. S13). Three hundred–nanometer beads (Ademtech Bio Adembeads) can also be imaged, but the background scattering starts to interfere with PSF of the bead. However, lowering the wavelength of the incident light to 450 nm allowed us to increase the intensity of the PSF and to strongly reduce the problem of background scattering (fig. S13D). Besides changing the wavelength of the incident light, tracking particles with a smaller scattering cross section would imply using more intense light sources displaying little speckles, such as mercury arc lamps (*5*), but the light intensity may damage living particles. Lasers could also be used, but given their high coherence, background removal post-processing would then be necessary to remove the speckle.

Compared to PSF engineering methods developed for fluorescence microscopy (*18*, *41*–*44*), SDI achieves an equivalent precision of localization per collected photon (fig. S14). However, it is important to note that SDI sacrifices the proportion of emitted photons that is collected by the camera to achieve dark field and to obtain a larger spatial spread of the PSF. These two features are indeed critical for the real-time tracking of scattering microparticles at subkilohertz frequency and subnanometer precision but are unnecessary for single-molecule fluorescence microscopy. In particular, in fluorescence experiments, dark field automatically arises from the wavelength filtering: This allows the use of phase masks instead of intensity masks and thus the maximization of the number of collected photons. In our case, the slits only collect 10 to 20% of the light scattered by a bead of diameter 1 μm. For very small particles, such as single molecules, the scattering would be isotropic, and this loss would be worse. For this reason, SDI is primarily a microparticle tracking method and is not intended to compete with existing single-molecule fluorescence techniques that were designed to maximize the number of collected photons. Photons are indeed far more precious for single-molecule fluorescence (typically 10^4 photons per second for an irradiance of the order of 1 kW/cm^2) than for microparticle tracking (in our case, 10^{10} photons per second at an irradiance close to 1 W/cm^2).

Last, it is noteworthy that the design of the slits and the corresponding angle of the illumination are important parameters that need to be adapted to the imaged particles. There are three parameters that have to be adjusted to the scatterer to be observed: their width, their length, and their separation. For a given averaged angle, a larger separation between the slits allows a better sensitivity and thus a better precision in the z direction but decreases the depth of field. Larger widths and lengths (however, fully contained inside the pupil of the objective) will increase the quantity of light that goes through the objective and thus the sensitivity to small particles but will also reduce the width of the PSF, as well as the depth of field of the signal. Once these three trade-offs are taken into account, the method is easy to learn and use, especially because it can be, as we showed, directly implemented to any existing microscope by engineering the objective. Furthermore, the signal analysis procedure, described in text S6, is simple and computationally inexpensive. For this reason, we claim that SDI has the ability to extensively increase the adoption of 3D tracking methods in the biological community, especially with the increase in quality and speed occurring in the camera field.

MATERIALS AND METHODS

Optics

Out-of-the-objective setup (40× and 100× objectives)

Superluminescent LEDs (Exalos, EXS210030-03, 650 nm, 10 mW) are placed in the object focal plane of a diode collimation package (LTN330A, Thorlabs), and the outcoming parallel beams are directed to the pupil of the oil objectives (UPLSAPO100X and UPLSAPO40X, respectively) with opposite incident angles. Their intensity is regulated through a feedback loop based on the signal of the monitor photodiode included in the chip. The optical axis is then switched from vertical to horizontal using a mirror (BBEA1-E0Z, Thorlabs). The 4f setup, used to access the Fourier plane, is made of two lenses of focal 100 mm (AC254, Thorlabs). A sheet of black paper (Canson, 160 g/m^2) is then cut with a laser machine to get the pair of slits needed for the SDI technique. Slits consist of four identical rectangles (200 μm by 700 μm) whose centers are placed at the following positions with respect to the optical axis: ([−1.5 mm,0],[−0.4 mm,0], [0.4 mm,0],[1.5 mm,0]). The slits are brought in contact with a thin lens of focal 100 mm (LBF254-100-A, Thorlabs). Then, a pair of optically clear glass slides (4 mm by 8 mm) of 1-mm thickness is placed in contact with this lens. Both are tilted in the y direction with opposite angles of ±17° to shift the beams stemming from both pair of slits in opposite y directions. Last, the resulting pattern is imaged on a monochromatic complementary metal-oxide semiconductor camera (UI-3060-CP-M, IDS uEye), placed at 100 mm from the titled glass slides. The camera is linked through USB3.1 to a computer that processes the images in real time. The protocol of the alignment is described in text S7.

Modified 20× objective

An achromatic 20× objective from Olympus was dismantled. We have replaced a cylindrical spacer 14 mm wide and 10 mm long just after the front lens component of the objective by a holder supporting a black paper with slits followed by prisms and a spacer so that this system also spans 10 mm. A round glass slide of radius 13 mm was inserted in the holder to hold the prisms. We have machined a (8 mm by 8 mm) rectangle slit in the holder allowing us to introduce two optically clear glass slides (4 mm by 8 mm) of thickness 1 mm in contact with the round one. One of the rectangular glass slides was slightly titled by introducing a thin sheet of paper of

thickness ≈10 μm (cigarette paper) between it and the round slide. The other rectangular glass slide was tilted in the opposite direction by introducing an identical sheet of paper on the opposite side. The space left between the round slide and the tiled rectangular slides was filled by capillarity with a drop of Olympus immersion oil to create two prisms of opposite angles. A sheet of black paper in which the SDI slits were cut was then added on top of the prisms. Slits consist of four rectangles whose centers are placed at the following positions with respect to the optical axis: ([−2.2 mm,0],[−0.9 mm,0],[0.9 mm,0],[2.2 mm,0]). Outer slits (width, 0.85 mm; height, 1.25 mm) are wider than inner slits (width, 0.55 mm; height, 1.25 mm) to compensate for the smaller light intensity at large scattering angles. The height of the cylindrical spacer was adjusted so that, once the objective is reassembled, the slits are located at the back focal plane of the objective (fig. S15). Lateral centering of the slits-containing mask is permitted by the interlocking shapes of the mask and its support (Fig. 3B).

Measurement of the optical noise of the setup

To accurately measure the optical noise of the setup and compare it to theory, it is necessary to uncouple it from the Brownian motion and from slow thermal or mechanical drifts that can affect the measurement. To do so, we melt MyOne T1 beads (Thermo Fisher Scientific) on a glass surface. The stock solution was diluted 10,000 times and then spread on a glass slide. The slide was then heated at 110°C for 5 min following the evaporation of the solution. A standard flow cell was then assembled with this slide, and water was injected. The position of 15 beads was then tracked for 5 s at 160 Hz at different light intensity. The average of the trajectory of the 15 beads was then subtracted from each trajectory to get rid of mechanical or thermal drifts.

Temperature control

To minimize optical drifts that are due to temperature changes, the objective is inserted into a box made of duralumin. The box temperature is controlled through six Peltier moduli placed in parallel (ET-063-08-15, Adaptive). The proportional–integral–derivative (PID) feedback loop then allows us to reach temperature stabilization with the precision of 0.0001 K. The temperature is read in the following way: Thermistors (TDK, B57703M0103) are connected to Wheatstone bridges converting the resistance difference into a voltage. The voltage is then read with a 32-bit Sigma-Delta analog-to-digital converter.

Focus adjustment

For the linearity test of the setup with 40× or 100× magnification, the objective is moved with a piezo nanofocusing device (P-725.2CL, Physik Instrumente). For the other measurements on this setup, the piezo nanofocusing device is replaced by a deformable stage to avoid any noise inherent to the piezoelectric device. The position of the screw controlling the stage is measured with a rotational magnetic sensor (AMS, AS5048A). For the linearity test of the 20× setup used for algae tracking, the objective is moved by the stepper motor driving the microscope focus (IX81, Olympus).

Single-molecule assays

All single-molecule experiments are performed at 25°C. All the DNA substrates used in the presented assays are synthesized ss oligonucleotides. Their sequences are indicated in table S1. Their 5′ end is complementary to a 57-base 3′ dibenzocyclooctyne (DBCO)–modified long oligonucleotide (Oli1) that is attached to azide-functionalized surfaces (PolyAn 2D Azide) through a 2-hour-long incubation (100 nM Oli1 and 500 mM NaCl). Their 3′ end is complementary to a 58-base oligonucleotide (Oli2). Oli2 contains two biotin modifications at its 5′ end. The ssDNA substrate is first hybridized with Oli2 by mixing both oligos at 100 nM in 100 mM NaCl and 30 mM tris-HCl (pH 7.6). Five microliters of streptavidin-coated Dynabeads MyOne T1 (Thermo Fisher Scientific) is washed three times in 200 μl of passivation buffer [140 mM NaCl, 3 mM KCl, 10 mM Na_2HPO_4, 1.76 mM KH_2PO_4, 2% bovine serum albumin, 2% Pluronic F-127, 5 mM EDTA, and 10 mM NaN_3 (pH 7.4)]. The result of the hybridization between the substrate and Oli2 is diluted down to 2 pM buffer and then incubated for 10 min with the beads in a total volume of 20 μl of passivation buffer. The beads are then rinsed three times with passivation buffer to remove unbound DNA. One microliter of the bead solution is then introduced in the cell coated with Oli1 and filled with passivation buffer. They are incubated for 5 min. Excess unbound beads are washed out by flowing passivation buffer.

Hybridization assay

The substrate used in these assays (HP10STACK) is a 153-base ssDNA strand. Once hybridized to Oli1 and Oli2, the size of the remaining ssDNA reduces to 38 bp. Twenty-four of these bases fold into a 10-bp hairpin with a four-base apex loop. This hairpin is used to test that only one DNA molecule is bound to the beads by testing the fluctuation between the open and closed state at 10 pN. Once this is checked, the hairpin is blocked by a 16-bp oligonucleotide (OliBlock-half-stack) for the half-stacked configuration or by a 22-bp oligonucleotide (Oliblock-full-stack) for the fully stacked configuration. The remaining bases of ssDNA contain the eight-base sequence that is complementary to the oligonucleotide whose hybridization kinetics is measured. The assay is realized in Hybridization Buffer [100 mM NaCl and 40 mM tris-HCl (pH 7.6)].

Upf1 stepping assays

A 193-base ssDNA is used in this assay (HP30). Once hybridized to Oli1 and Oli2, the size of the ssDNA reduces to 78 bases. Among them, a 30-bp hairpin is included with a loop of four bases. It is flanked by two handles of seven successive thymines. Once the beads are attached to the surface of the cell, the buffer is changed to Upf1 buffer [100 mM KCl, 3 mM $MgCl_2$, and 40 mM tris-HCl (pH 7.6)]. The closing and opening of the hairpin are tested using a force scan going from 20 to 8 pN. The force is then fixed to 8 pN on average, and the helicase domain of yeast-Upf1 purified as described in (*29*) is injected with ATP in Upf1 buffer at a concentration of 10 nM unless otherwise mentioned.

DNA hairpin folding assay

The substrate used in this assay (HP10FLUC) is a 160-base-long ssDNA strand. Once hybridized to Oli1 and Oli2, the size of the remaining ssDNA reduces to 45 bases. Twenty-four of these bases fold into a 10-bp hairpin with a 4-base apex loop. The kinetic of the folding and unfolding transitions of the hairpin at different forces is acquired in passivation buffer.

Cultures of microorganisms and microfluidic experiments

Cultures of *C. reinhardtii* strain CC125 were grown axenically in a tris-acetate-phosphate (TAP) medium at 20°C under periodic fluorescent illumination (≈100 μE m^2 s^{-1}; cycle: 16-hour light/8-hour dark). Cells were harvested in the exponentially growing phase and then centrifuged at 800 rpm for 10 min, and the supernatants were

replaced with fresh TAP. A dilute suspension ($\approx 10^{-5}$%) was then loaded into a simple microfluidic chip ($L \approx 1$ cm, $W \approx 3$ mm, and $H = 150$ μm; made with standard soft photolithography techniques) where the algae dynamic was acquired at 10 fps (camera uEye UI-3000SE) on an inverted IX81 Olympus microscope with the SDI objective described in the section "Direct incorporation into a pre-existing microscope" and using a 730-nm LED for illumination to prevent phototactic responses from the cells.

Image analysis

Images are transmitted in real time to a computer and analyzed on the fly at the frequencies indicated in the Results section. For high-magnification and high-precision applications (force spectroscopy), images are analyzed through Fourier decomposition using the algorithm described in text S6. Eventual optomagnetic misalignments are corrected as indicated in text S8. In the case of algae tracking, the position of the fringes is simply measured through the computation of the barycenter of their intensity in the x and y directions, and the resulting signal is processed through a finite impulse response filter of 0.8-s width (eight frames).

SUPPLEMENTARY MATERIALS

Supplementary material for this article is available at http://advances.sciencemag.org/cgi/content/full/7/6/eabe3902/DC1

View/request a protocol for this paper from *Bio-protocol*.

REFERENCES AND NOTES

1. H. C. Berg, D. A. Brown, Chemotaxis in *Escherichia coli* analysed by three-dimensional tracking. *Nature* **239**, 500–504 (1972).
2. S. Hodeib, S. Raj, M. Manosas, W. Zhang, D. Bagchi, B. Ducos, J.-F. Allemand, D. Bensimon, V. Croquette, Single molecule studies of helicases with magnetic tweezers. *Methods* **105**, 3–15 (2016).
3. T. B. Brouwer, N. Hermans, J. van Noort, Multiplexed nanometric 3D tracking of microbeads using an FFT-phasor algorithm. *Biophys. J.* **118**, 2245–2257 (2020).
4. D. Dulin, T. J. Cui, J. Cnossen, M. W. Docter, J. Lipfert, N. H. Dekker, High spatiotemporal-resolution magnetic tweezers: Calibration and applications for DNA dynamics. *Biophys. J.* **109**, 2113–2125 (2015).
5. A. Huhle, D. Klaue, H. Brutzer, P. Daldrop, S. Joo, O. Otto, U. F. Keyser, R. Seidel, Camera-based three-dimensional real-time particle tracking at kHz rates and Ångström accuracy. *Nat. Commun.* **6**, 5885 (2015).
6. A. von Diezmann, Y. Shechtman, W. E. Moerner, Three-dimensional localization of single molecules for super-resolution imaging and single-particle tracking. *Chem. Rev.* **117**, 7244–7275 (2017).
7. E. A. Abbondanzieri, W. J. Greenleaf, J. W. Shaevitz, R. Landick, S. M. Block, Direct observation of base-pair stepping by RNA polymerase. *Nature* **438**, 460–465 (2005).
8. B. M. Lansdorp, S. J. Tabrizi, A. Dittmore, O. A. Saleh, A high-speed magnetic tweezer beyond 10,000 frames per second. *Rev. Sci. Instrum.* **84**, 044301 (2013).
9. J. Hanne, G. Zocchi, N. K. Voulgarakis, A. R. Bishop, K. Ø. Rasmussen, Opening rates of DNA hairpins: Experiment and model. *Phys. Rev. E* **76**, 011909 (2007).
10. H. Brutzer, F. W. Schwarz, R. Seidel, Scanning evanescent fields using a pointlike light source and a nanomechanical DNA gear. *Nano Lett.* **12**, 473–478 (2012).
11. E. T. Graves, C. Duboc, J. Fan, F. Stransky, M. Leroux-Coyau, T. R. Strick, A dynamic DNA-repair complex observed by correlative single-molecule nanomanipulation and fluorescence. *Nat. Struct. Mol. Biol.* **22**, 452–457 (2015).
12. K. M. Taute, S. Gude, S. J. Tans, T. S. Shimizu, High-throughput 3D tracking of bacteria on a standard phase contrast microscope. *Nat. Commun.* **6**, 8776 (2015).
13. C. Gosse, V. Croquette, Magnetic tweezers: Micromanipulation and force measurement at the molecular level. *Biophys. J.* **82**, 3314, 3329 (2002).
14. D. Baddeley, M. B. Cannell, C. Soeller, Three-dimensional sub-100 nm super-resolution imaging of biological samples using a phase ramp in the objective pupil. *Nano Res.* **4**, 589, 589 (2011).
15. Y. Shechtman, S. J. Sahl, A. S. Backer, W. E. Moerner, Optimal point spread function design for 3D imaging. *Phys. Rev. Lett.* **113**, 133902 (2014).
16. H. P. Kao, A. S. Verkman, Tracking of single fluorescent particles in three dimensions: Use of cylindrical optics to encode particle position. *Biophys. J.* **67**, 1291–1300 (1994).
17. B. Huang, W. Wang, M. Bates, X. Zhuang, Three-dimensional super-resolution imaging by stochastic optical reconstruction microscopy. *Science* **319**, 810–813 (2008).
18. S. R. P. Pavani, M. A. Thompson, J. S. Biteen, S. J. Lord, N. Liu, R. J. Twieg, R. Piestun, W. E. Moerner, Three-dimensional, single-molecule fluorescence imaging beyond the diffraction limit by using a double-helix point spread function. *Proc. Natl. Acad. Sci. U.S.A.* **106**, 2995–2999 (2009).
19. S. Jia, J. C. Vaughan, X. Zhuang, Isotropic 3D super-resolution imaging with a self-bending point spread function. *Nat. Photonics* **8**, 302–306 (2014).
20. K. Kim, O. A. Saleh, A high-resolution magnetic tweezer for single-molecule measurements. *Nucleic Acids Res.* **37**, e136 (2009).
21. R. W. Taylor, R. G. Mahmoodabadi, V. Rauschenberger, A. Giessl, A. Schambony, V. Sandoghdar, Interferometric scattering microscopy reveals microsecond nanoscopic protein motion on a live cell membrane. *Nat. Photonics* **13**, 480–487 (2019).
22. Y. Sun, J. D. M. Kenna, J. M. Murray, E. M. Ostap, Y. E. Goldman, *Parallax*: High accuracy three-dimensional single molecule tracking using split images. *Nano Lett.* **9**, 2676–2682 (2009).
23. Y. Sun, O. Sato, F. Ruhnow, M. E. Arsenault, M. Ikebe, Y. E. Goldman, Single-molecule stepping and structural dynamics of myosin X. *Nat. Struct. Mol. Biol.* **17**, 485–491 (2010).
24. G. Sancataldo, L. Scipioni, T. Ravasenga, L. Lanzanò, A. Diaspro, A. Barberis, M. Duocastella, Three-dimensional multiple-particle tracking with nanometric precision over tunable axial ranges. *Optica* **4**, 367–373 (2017).
25. V. Croquette, J.-F. Allemand, T. Vielle, Optical device for measuring the position of an object, U.S. Patent 9,933,609 (2018).
26. P. Yakovchuk, E. Protozanova, M. D. Frank-Kamenetskii, Base-stacking and base-pairing contributions into thermal stability of the DNA double helix. *Nucleic Acids Res.* **34**, 564–574 (2006).
27. K. D. Whitley, M. J. Comstock, Y. R. Chemla, Elasticity of the transition state for oligonucleotide hybridization. *Nucleic Acids Res.* **45**, 547–555 (2017).
28. F. Fiorini, D. Bagchi, H. L. Hir, V. Croquette, Human Upf1 is a highly processive RNA helicase and translocase with RNP remodelling activities. *Nat. Commun.* **6**, 7581 (2015).
29. J. Kanaan, S. Raj, L. Decourty, C. Saveanu, V. Croquette, H. L. Hir, UPF1-like helicase grip on nucleic acids dictates processivity. *Nat. Commun.* **9**, 3752 (2018).
30. W. Cheng, S. G. Arunajadai, J. R. Moffitt, I. Tinoco Jr., C. Bustamante, Single–base pair unwinding and asynchronous RNA release by the hepatitis C virus NS3 helicase. *Science* **333**, 1746–1749 (2011).
31. M. Brun-Cosme-Bruny, Swimming of active suspensions in a crowded environment, thesis, Université Grenoble Alpes (2019).
32. V. Kantsler, J. Dunkel, M. Polin, R. E. Goldstein, Ciliary contact interactions dominate surface scattering of swimming eukaryotes. *Proc. Natl. Acad. Sci. U.S.A.* **110**, 1187–1192 (2013).
33. M. Polin, I. Tuval, K. Drescher, J. P. Gollub, R. E. Goldstein, *Chlamydomonas* swims with two "gears" in a eukaryotic version of run-and-tumble locomotion. *Science* **325**, 487–490 (2009).
34. V. Kam, N. Moseyko, J. Nemson, L. J. Feldman, Gravitaxis in *Chlamydomonas reinhardtii*: Characterization using video microscopy and computer analysis. *Int. J. Plant Sci.* **160**, 1093–1098 (1999).
35. T. J. Pedley, J. O. Kessler, Hydrodynamic phenomena in suspensions of swimming microorganisms. *Annu. Rev. Fluid Mech.* **24**, 313–358 (1992).
36. Z. Qi, R. A. Pugh, M. Spies, Y. R. Chemla, Sequence-dependent base pair stepping dynamics in XPD helicase unwinding. *eLife* **2**, e00334 (2013).
37. M. Spies, Two steps forward, one step back: Determining XPD helicase mechanism by single-molecule fluorescence and high-resolution optical tweezers. *DNA Repair* **20**, 58–70 (2014).
38. F. Mosconi, J. F. Allemand, V. Croquette, Soft magnetic tweezers: A proof of principle. *Rev. Sci. Instrum.* **82**, 034302 (2011).
39. D. Klaue, R. Seidel, Torsional stiffness of single superparamagnetic microspheres in an external magnetic field. *Phys. Rev. Lett.* **102**, 028302 (2009).
40. H. Brenner, The slow motion of a sphere through a viscous fluid towards a plane surface. *Chem. Eng. Sci.* **16**, 242–251 (1961).
41. B. J. Sumlin, W. R. Heinson, R. K. Chakrabarty, Retrieving the aerosol complex refractive index using PyMieScatt: A Mie computational package with visualization capabilities. *J. Quant. Spectrosc. Radiat. Transf.* **205**, 127–134 (2018).
42. M. J. Mlodzianoski, M. F. Juette, G. L. Beane, J. Bewersdorf, Experimental characterization of 3D localization techniques for particle-tracking and super-resolution microscopy. *Opt. Express* **17**, 8264–8277 (2009).
43. L. Holtzer, T. Meckel, T. Schmidt, Nanometric three-dimensional tracking of individual quantum dots in cells. *Appl. Phys. Lett.* **90**, 053902 (2007).
44. M. D. Lew, S. F. Lee, M. Badieirostami, W. E. Moerner, Corkscrew point spread function for far-field three-dimensional nanoscale localization of pointlike objects. *Opt. Lett.* **36**, 202–204 (2011).
45. P. Bon, J. Linarès-Loyez, M. Feyeux, K. Alessandri, B. Lounis, P. Nassoy, L. Cognet, Self-interference 3D super-resolution microscopy for deep tissue investigations. *Nat. Methods* **15**, 449–454 (2018).

46. R. E. Thompson, D. R. Larson, W. W. Webb, Precise nanometer localization analysis for individual fluorescent probes. *Biophys. J.* **82**, 2775–2783 (2002).
47. J. Opfer, K.-E. Gottschalk, Identifying discrete states of a biological system using a novel step detection algorithm. *PLOS ONE* **7**, e45896 (2012).
48. A. J. Goldman, R. G. Cox, H. Brenner, Slow viscous motion of a sphere parallel to a plane wall—I Motion through a quiescent fluid. *Chem. Eng. Sci.* **22**, 637–651 (1967).

Acknowledgments: This work has originated in collaboration with T. Dupic. We wish to acknowledge stimulating discussions with H. Le Hir, J. Ouellet, D. Bensimon, N. Desprat, D. Fangyuan, M. Manosas, and F. Hamouri and help with hairpins and dsDNA constructs. **Funding:** This study was supported by the ANR CLEANMD grant (ANR-14-CE10-0014) and ANR G4-CRASH (ANR-19-CE11-0021-01) from the French Agence Nationale de la Recherche to V.C., by the European Research Council grant Magreps [267 862] to V.C. Work in the group of V.C. is part of "Institut Pierre-Gilles de Gennes" ("Investissements d'Avenir" program ANR-10-IDEX-0001-02 PSL and ANR-10-LABX-31) and the Qlife Institute of Convergence (Université PSL). **Author contributions:** M.R. designed, performed, and analyzed the biological experiments; performed the signal treatment and the theoretical analysis; contributed to the setup; and wrote the manuscript. T.V. built, calibrated, and characterized the optical setup and contributed significantly to its design. G.R. built the electronics. T.V. and G.R. built the mechanics. N.R.-G. expressed and purified Upf1. B.D. contributed to the purification of DNA substrates. R.J. performed the culture of *C. reinhardtii* and supervised the analysis of their trajectories. V.C. supervised the research; designed the optical setup, its mechanics, and its electronics; and contributed to its experimental implementation. J.-F.A. contributed to the design of the experiments and helped supervise the project. All authors discussed the results and commented on the manuscript. **Competing interests:** V.C., T.V., and J.-F.A. are inventors on a patent related to this work filed by the Universite Pierre et Marie Curie Paris (no. US9933609B2, published 3 April 2018). J.-F.A. and V.C. own shares of the company Depixus that makes a commercial use of SDI. T.V. and G.R. are now employed by the same company. The authors declare that they have no other competing interests. **Data and materials availability:** Processed data supporting the conclusions of this study are all shown in the manuscript. Raw data generated during the work are available from the corresponding author on reasonable request. All data needed to evaluate the conclusions in the paper are present in the paper and/or the Supplementary Materials.

Submitted 18 August 2020
Accepted 18 December 2020
Published 5 February 2021
10.1126/sciadv.abe3902

Citation: M. Rieu, T. Vieille, G. Radou, R. Jeanneret, N. Ruiz-Gutierrez, B. Ducos, J.-F. Allemand, V. Croquette, Parallel, linear, and subnanometric 3D tracking of microparticles with Stereo Darkfield Interferometry. *Sci. Adv.* **7**, eabe3902 (2021).

Science Advances

Parallel, linear, and subnanometric 3D tracking of microparticles with Stereo Darkfield Interferometry

Martin Rieu, Thibault Vieille, Gaël Radou, Raphaël Jeanneret, Nadia Ruiz-Gutierrez, Bertrand Ducos, Jean-François Allemand and Vincent Croquette

Sci Adv **7** (6), eabe3902.
DOI: 10.1126/sciadv.abe3902